Intensified Diurnal Tides along the Oregon Coast

Citation	Osborne, J. J., Kurapov, A. L., Egbert, G. D., & Kosro, P. M. (2014). Intensified Diurnal Tides Along the Oregon Coast. Journal of Physical Oceanography, 44(7), 1689-1703. doi:10.1175/JPO-D-13-0247.1
DOI	10.1175/JPO-D-13-0247.1
Publisher	American Meteorological Society
Version	Version of Record
Terms of Use	http://cdss.library.oregonstate.edu/sa-termsofuse

Intensified Diurnal Tides along the Oregon Coast

J. J. OSBORNE, A. L. KURAPOV, G. D. EGBERT, AND P. M. KOSRO

College of Earth, Ocean, and Atmospheric Sciences, Oregon State University, Corvallis, Oregon

(Manuscript received 12 November 2013, in final form 30 January 2014)

ABSTRACT

Intensified diurnal tides are found along portions of the Oregon shelf (U.S. West Coast) based on analyses of high-frequency (HF) radar surface current data and outputs of a 1-km resolution ocean circulation model. The K_1 tidal currents with magnitudes near 0.07 m s^{-1} over a wider part of the shelf (Heceta Bank complex; 44°–44.5°N), previously predicted by Erofeeva et al., are confirmed here by newly available HF radar data. Intensified diurnal tides are also found along the narrow shelf south of Heceta Bank. In the close vicinity of Cape Blanco (42.8°N), diurnal tidal currents (K_1 and O_1 constituents combined) may reach 0.3 m s^{-1}. Appreciable differences in diurnal tide intensity are found depending on whether the model is forced with tides and winds (TW) or only tides. Also, diurnal variability in wind forcing is found to affect diurnal surface velocities. For the case forced by tides alone, results strongly depend on whether the model ocean is stratified [tides only, stratified (TOS)] or not [tides only, no stratification (TONS)]. In case TONS, coastal-trapped waves at diurnal frequencies do not occur over the narrow shelf south of 43.5°N, consistent with the dispersion analysis of a linear shallow-water model. However, in case TOS, diurnal tides are intensified in that area, associated with the presence of coastal-trapped waves. Case TW produces the strongest modeled diurnal tidal motions over the entire Oregon shelf, partially due to cross-shore tidal displacement (advection) of alongshore subinertial currents. At Cape Blanco, diurnal tidal variability dominates the modeled relative vorticity spectrum, suggesting that tides may influence the separation of the alongshore coastal jet at that location.

1. Introduction

Summer circulation off the Oregon coast is characterized by wind-driven coastal upwelling varying on temporal scales of several days, driving a southward jet with a mean speed near 0.5 m s^{-1}. As summer progresses, the cold SST front (Fig. 1a) is driven offshore by Ekman transport, eddy variability, and separating coastal jets. Tides are dominated by the M_2 constituent (period of 12.42 h), with barotropic (depth averaged) currents of up to 0.06 m s^{-1} over the shelf and internal tides reaching 0.15 m s^{-1} (Hayes and Halpern 1976; Torgrimson and Hickey 1979; Erofeeva et al. 2003; Kurapov et al. 2003; Osborne et al. 2011). Energetic diurnal tidal currents may also occur locally along the Oregon coast. A data-assimilating shallow-water ocean tidal model (Erofeeva et al. 2003) suggests that K_1 tidal currents (period of 23.93 h) may exceed 0.10 m s^{-1} over the wide Heceta Bank portion of the Oregon shelf (44°–45°N). Reexamining historical current-meter data, Erofeeva et al. (2003) also found that O_1 currents could reach up to 0.08 m s^{-1}. The intensification of K_1 currents was attributed to coastal-trapped waves at a subinertial diurnal tide frequency. These have been associated with intensified diurnal tides in several places around the world, for example, St. Kilda Island, United Kingdom (Cartwright 1969), Vancouver Island, Canada (Crawford and Thomson 1982; Cummins et al. 2000), and the Sea of Okhotsk, Russia (Kovalev and Rabinovich 1980; Yefimov and Rabinovich 1980; Rabinovich and Zhukov 1984; Odamaki 1994; Rabinovich and Thomson 2001).

While tidal currents are usually less energetic than wind-driven currents off Oregon, our recent model results using a comprehensive three-dimensional coastal ocean model (described in section 2) reveal that the shape of the SST front may be sensitive to details of barotropic tidal forcing. Cases using atmospheric forcing only (Fig. 1b), atmospheric forcing plus M_2 tides along the open boundaries (Fig. 1c), or atmospheric forcing plus eight tidal constituents (from shortest to longest period: K_2, S_2, M_2, N_2, K_1, P_1, O_1, and Q_1; Fig. 1d) yield, after 5 months of simulation, SST fronts of a quite

Corresponding author address: John Osborne, College of Earth, Ocean, and Atmospheric Sciences, Oregon State University, 104 CEOAS Administration Building, Corvallis, OR 97331.
E-mail: josborne@coas.oregonstate.edu

DOI: 10.1175/JPO-D-13-0247.1

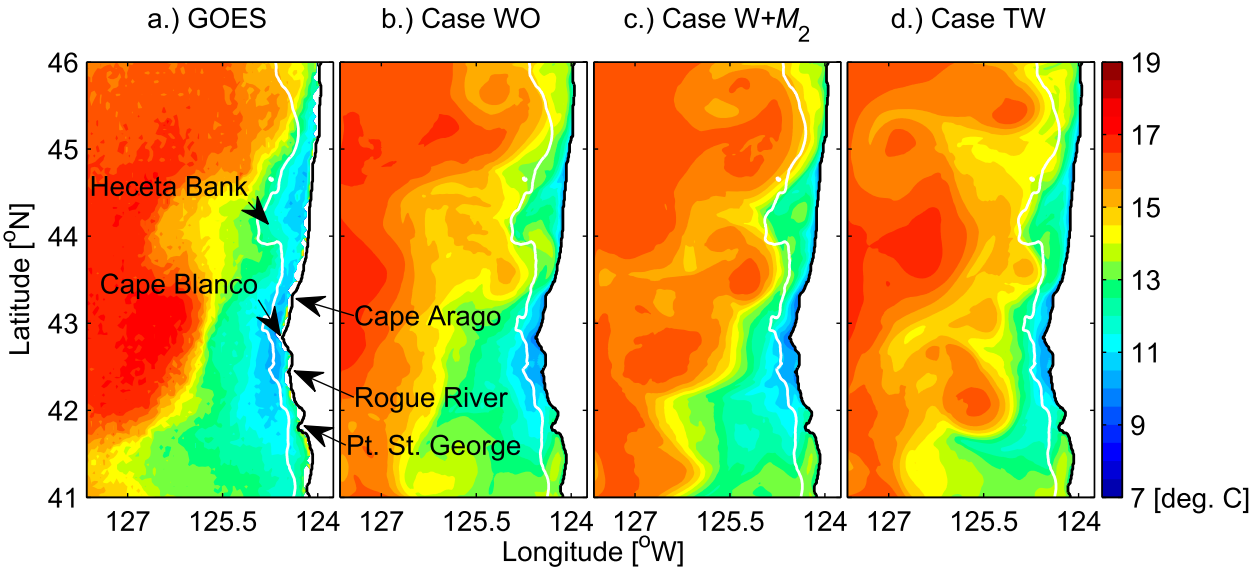

FIG. 1. August 2002 mean SST: (a) GOES observations (Maturi et al. 2008), (b) ROMS forced by winds only (case WO), (c) ROMS forced by winds and the M_2 tide (case W + M_2), and (d) ROMS forced by winds and eight tidal constituents (case TW). White lines mark the 200-m isobath. Selected geographical features are indicated.

different shape. For comparison, the observed August 2002 SST field [from the Geostationary Operational Environmental Satellite (GOES) observations; Maturi et al. 2008] is shown in Fig. 1a. While differences in the SST front geometry possibly reflect the high sensitivity of the nonlinear hydrostatic model to small changes in the boundary conditions (Oliger and Sundström 1978), it is also possible that tides influence dynamics at subtidal frequencies, for example, affecting coastal jet separation and offshore transport. This sensitivity has motivated us to look closer at diurnal tides using model results and surface currents observed by high-frequency (HF) radars (HFR). Strong observed and modeled diurnal currents are found in the area identified by Erofeeva et al. (2003) (section 3). Large tidal velocities are also found near Cape Blanco (see Fig. 1), resulting from a combination of mechanisms discussed in sections 4 and 5, including coastal-trapped waves and the cross-shore advection of the subinertial alongshore jet by the diurnal tidal current.

2. Model

The model is based on the Regional Ocean Modeling System (ROMS; Shchepetkin and McWilliams 2005; www.myroms.org) that describes nonlinear evolution of stratified flows using hydrostatic and Boussinesq approximations. Use of terrain-following coordinates in the vertical makes it particularly suitable for shelf flow studies, because the surface and bottom boundary layers can be finely resolved. Details of the implementation used here are very similar to Osborne et al. (2011). The model domain is (41°–46°N, 127.6°W–coast), with a resolution of 1 km in the horizontal and 40 terrain-following levels in the vertical. The study period is from April through August 2002. Unless noted, winds are daily averages from the Coupled Ocean–Atmosphere Mesoscale Prediction System (COAMPS; Hodur 1997), and parameters for surface heat flux computation are monthly averages from the National Centers for Environmental Prediction (NCEP) reanalysis (Kalnay et al. 1996). The daily averaged winds are used to remove atmospheric diurnal variability, isolating diurnal tides as the only forcing mechanism with a 24-h period. An additional model run is done using high-frequency (hourly resolution) winds to assess the response of near-surface currents to diurnal atmospheric variability. Subtidal boundary conditions are obtained from a 3-km regional ocean circulation model (Koch et al. 2010) and barotropic tides from a U.S. West Coast 1/30° shallow-water data-assimilating model (Egbert and Erofeeva 2002; http://volkov.oce.orst.edu/tides/). Tidal forcing is applied by periodically varying (at each of the eight tidal frequencies) the velocity and sea surface height along the boundaries. No tidal forcing is applied at interior grid points. Several cases are considered below. The case "tides plus winds" (TW) is forced by the winds, atmospheric heat fluxes, and the eight dominant tidal constituents. The case "tides only, no stratification" (TONS) is forced by tides only and simulates the response of the

unstratified ocean that has zero initial velocity. The case ''tides only, stratified'' (TOS) is forced by tides only applied to the stratified ocean, which was initially at the state of rest (zero velocities and horizontally uniform stratification corresponding to average summer conditions off Oregon; Smith et al. 2001). Instantaneous model outputs are saved hourly for subsequent filtering and harmonic analysis.

3. Case TW: Comparison against high-frequency radar surface currents

Erofeeva et al. (2003) noted local intensification of K_1 and O_1 currents over the broader portion of the Oregon shelf between 44° and 45°N (Heceta and Stonewall Banks). In their study, surface velocities from short-range (40 km) HF radars were assimilated, but those data did not cover the entire Heceta Bank area. The strongest modeled K_1 tides were more than 40 km from the radar, thus no direct observational evidence was available at that time to confirm the strongest model K_1 tides. Surface current data from three 150-km long-range HF radars with overlapping coverage are now available in this region (Figs. 2a–c and 3a–c; Kosro 2005; Kosro et al. 2006; Saraceno et al. 2008), located at 42.84°N [Cape Blanco Long (CBL)], 43.67°N [Winchester Bay (WIN)], and 44.68°N [Yaquina Head Long (YHL)]. We analyze hourly observations from CBL and WIN for June–August 2002 (92 days) and hourly observations from YHL (installed later) for June–July 2008 (61 days). Crawford and Thomson (1984) conclude that seasonally varying ocean conditions (currents and stratification) may have a significant impact on diurnal tides. Comparisons using model outputs and data from different years are justified because they are from the same time of year. Each radar senses the radial component of the surface currents, along the line from the radar to the measurement point. While maps of two orthogonal velocity components (i.e., east–west/north–south) can be obtained in areas of overlapping coverage, we choose to analyze the radial velocity component data here, because they provide more uniform accuracy (no issue with geometric dilution of precision) and better resolution.

The HF radar radial velocity component time series have been harmonically analyzed using the T_TIDE software package (Pawlowicz et al. 2002). We infer for the P_1 constituent, as none of the time series are long enough to separate the P_1 and K_1 constituents (178-day beat period). Here, we provide analysis of both the K_1 and O_1 tidal amplitudes. The observed K_1 signal is stronger than O_1, but may be contaminated by diurnal wind-driven variability. The diurnal wind frequency differs from the K_1 frequency by 1 cpy, such that signals at these two frequencies are difficult to separate in 2–3-month time series. The diurnal wind stress variability can be relatively large in the vicinity of Heceta Bank, as compared to the daily mean over the summer season. Perlin et al. (2004) examined twice-daily Quick Scatterometer (QuikSCAT; Liu 2002; Liu and Xie 2001) observations from June to September during 2000 and 2001 and found that the mean difference between mooring and evening winds may be as large as 0.04 N m^{-2} over a vast area of the Oregon shelf and slope, extending as far as 100 km offshore.

The observed O_1 signal, though weaker than the K_1 signal, is more easily separated from atmospherically forced diurnal signals. Comparing maps of diurnal current amplitudes at the K_1 and O_1 frequencies, we will attempt to delineate areas influenced by the tides and diurnal atmospheric variability.

Observed harmonic amplitudes are plotted in Fig. 2 (left) and Fig. 3 (left) for the K_1 and O_1 constituents, respectively. The K_1 observations between 44° and 45°N (Figs. 2a,b) show large areas with radial currents up to 0.05 m s^{-1}, qualitatively consistent with the results of the data-assimilating shallow-water tidal model of Erofeeva et al. (2003). Observed O_1 currents in this area are up to 0.04 m s^{-1}. Radial current amplitudes from YHL and WIN over the shelf near 44.5°N differ. The K_1 and O_1 tidal currents are north–south polarized in this area. This makes them nearly orthogonal to the radial direction of the YHL radar, but better aligned with the radial direction of the WIN radar. The strongest K_1 and O_1 radial velocity amplitudes are observed near Cape Blanco (see Figs. 2c and 3c), where K_1 amplitudes are in excess of 0.08 m s^{-1} and O_1 amplitudes are up to 0.05 m s^{-1}.

Areas of intensified O_1 tidal currents observed by the HF radars generally repeat those of K_1, with smaller amplitudes (cf. Figs. 2a–c and 3a–c). An exception is the shelf area north of 44.7°N sensed by the YHL instrument (cf. Figs. 2a and 3a), where K_1 currents are amplified and O_1 currents are not. Similarly, in the region offshore of the 200-m isobath between 43.4° and 43.9°N, the observed K_1 amplitudes (Fig. 2b) are much larger than O_1 (Fig. 3b). Perlin et al. (2004) find large diurnal variability in wind stress in these areas, and thus we suggest diurnal wind variability may contribute here to the diurnal variability in currents.

To compare the model solution to HF radar observations, model surface current velocities are interpolated to HFR observation locations, projected in the direction of HF radials, high-pass filtered, and then harmonically analyzed with T_TIDE. We first consider model cases forced with daily averaged wind

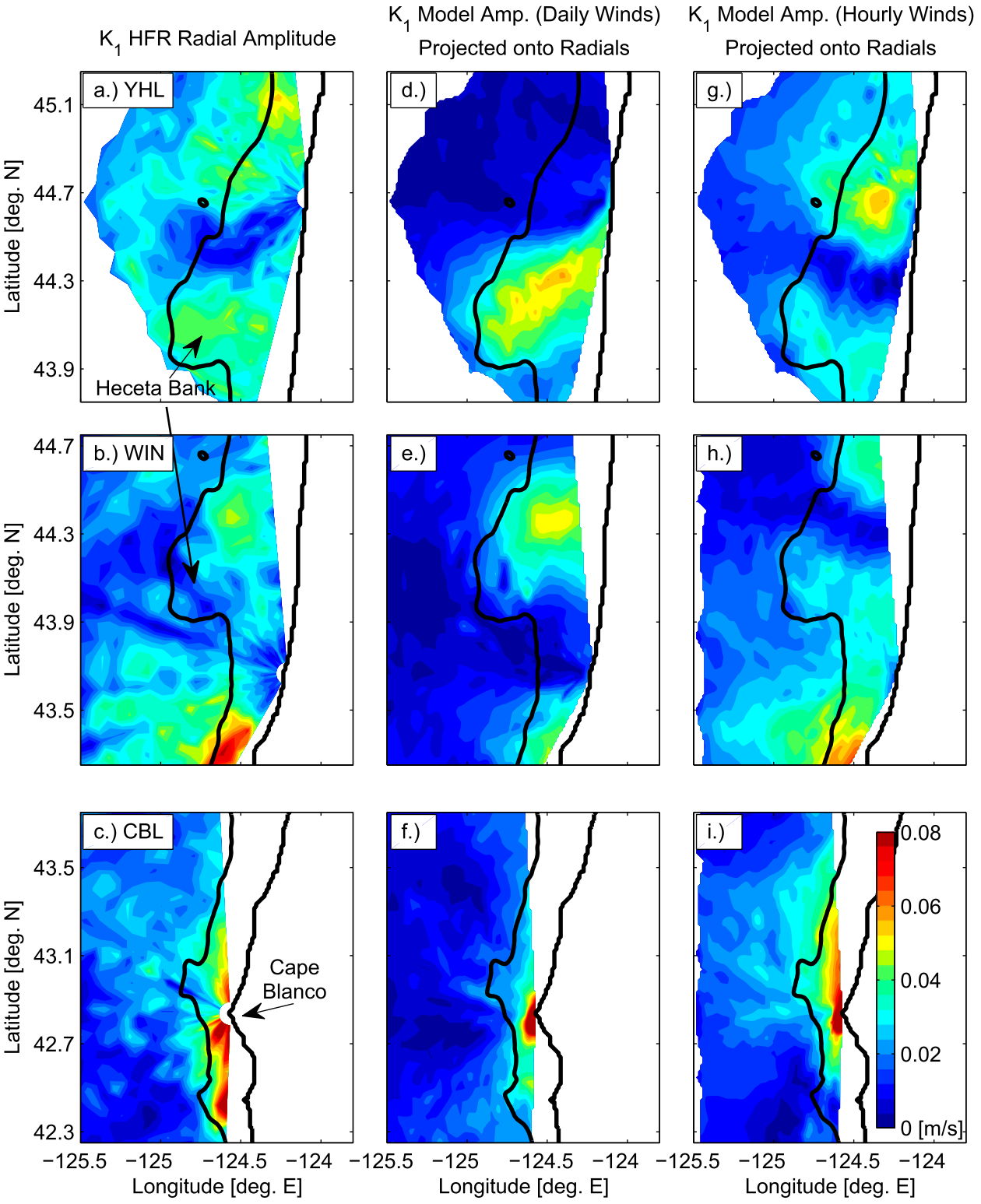

FIG. 2. Tidal amplitudes ($m\,s^{-1}$) of K_1 surface current radial amplitudes from (a)–(c) HFR, (d)–(f) model forced with daily averaged winds, and (g)–(i) HF (hourly) winds. This is given for YHL (top), WIN (middle), and CBL (bottom) radar. YHL observations are from June and July 2008, the first year such observations are available. WIN and CBL observations are from June to August 2002, the same year as the model. Black lines mark the 200-m isobath and the coast.

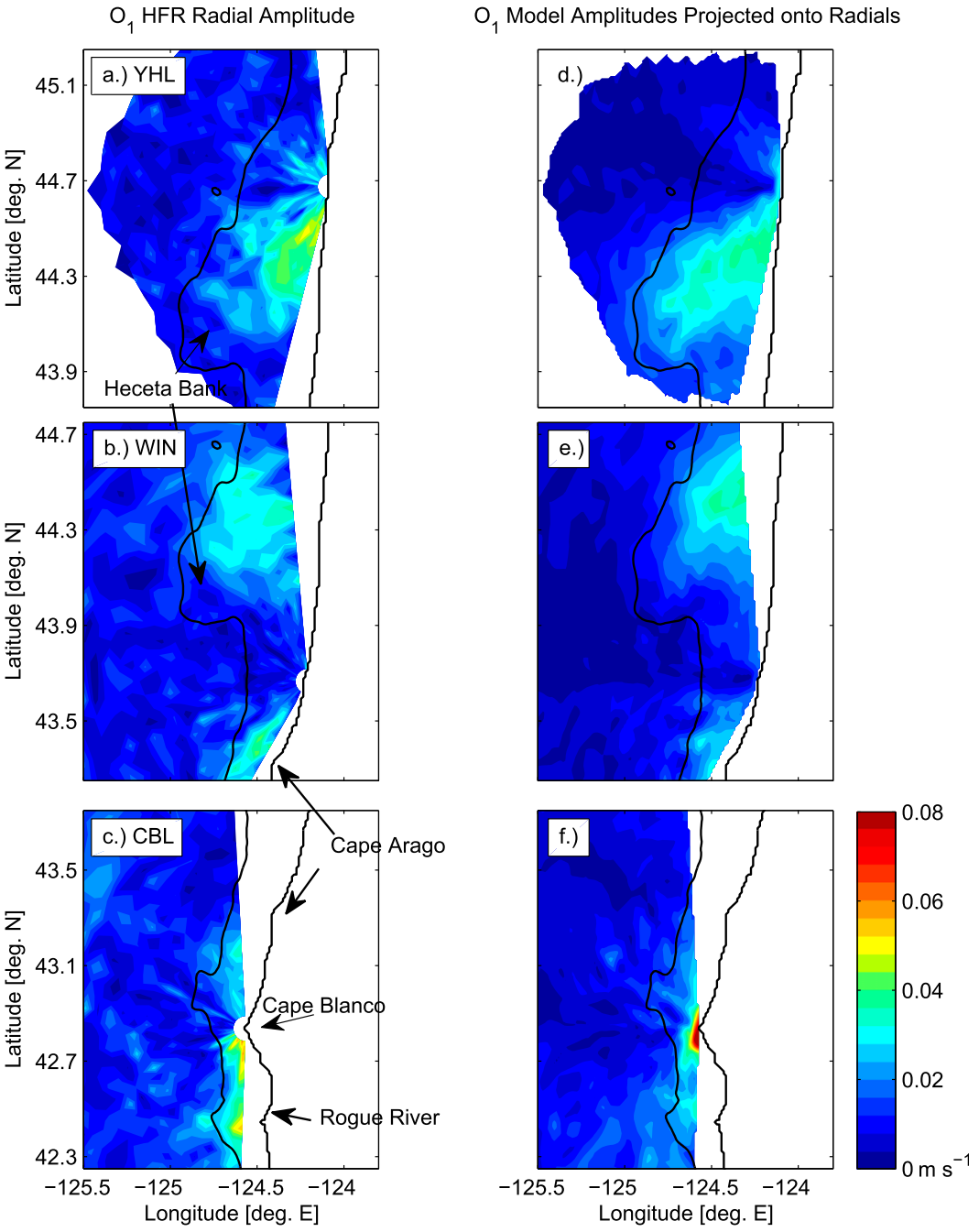

FIG. 3. As in Fig. 2a–f, but for O_1 currents. Tidal amplitudes (m s^{-1}) of O_1 surface current radial amplitudes from (a)–(c) HFR and (d)–(f) daily averaged wind model. This is given for YHL (top), WIN (middle), and CBL (bottom) radar. YHL observations are from June and July 2008, the first year such observations are available. WIN and CBL observations are from June to August 2002, the same year as the model. Black lines mark the 200-m isobath and the coast.

fields (Figs. 2d–f and 3d–f). Harmonic amplitudes of the model and HF radar K_1 and O_1 velocity radial components qualitatively agree with each other. Model K_1 amplitudes also agree with the model results of Erofeeva et al. (2003). In the coastal region north of 44.7°N and offshore region south of 43.9°N, where observed increased diurnal variability in K_1 estimates may possibly be driven by the atmospheric forcing (Figs. 2a–c), the modeled K_1 currents are small (see Figs. 2d–f). Because the diurnal variability is removed

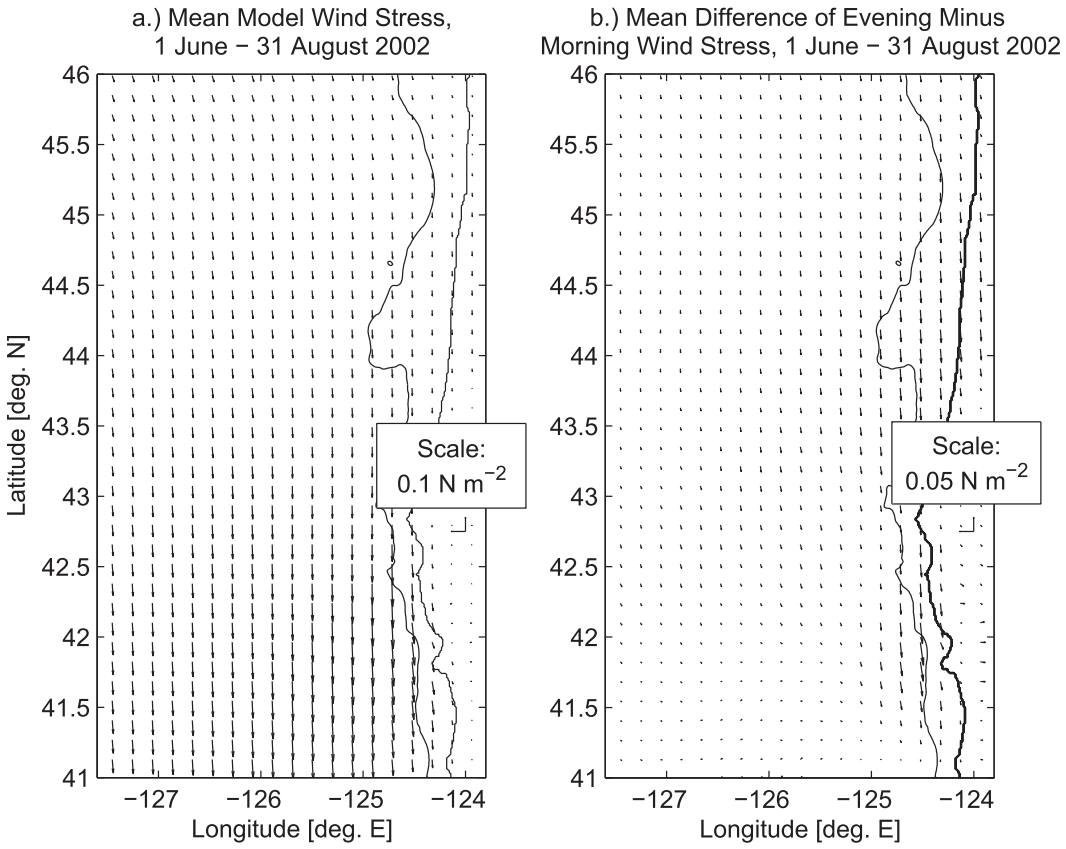

FIG. 4. (a) Mean model wind stress for 1 Jun–31 Aug 2002. (b) Mean of the differences of local evening (0300 UTC) and local morning (1800 UTC) wind stress for 1 Jun–31 Aug 2002. Note the difference in scales. The 200-m isobath and coast are contoured.

from the model wind forcing, finding that model amplitudes are weaker than observed amplitudes is also consistent with the hypothesis of atmospherically driven diurnal surface velocity variability in these two areas. As an additional indication, modeled O_1 amplitudes in the above-mentioned locations agree with observations (Fig. 3).

To further test the hypothesis of atmospherically driven diurnal surface velocity variability, we have computed a solution forced with high-frequency (hourly) winds. The mean wind stress field, June–August 2002, is shown in Fig. 4a and the mean difference in wind stress between 2000 LT (0300 UTC) and 1100 LT (1800 UTC) in Fig. 4b. Wind stress magnitudes near Heceta Bank vary by up to a factor of 2 over the course of a day, from 0.02 to 0.07 N m^{-2}.

The K_1 model radial component amplitudes using the high-frequency wind solution are shown in Figs. 2g–i. Between 42.7° and 44.3°N and 44.5° and 45.2°N, larger model amplitudes are found offshore of the 200-m isobath than in the case with daily averaged winds, in better agreement with HF radar observations. Amplitudes are also larger over the shelf north of 44.7°N and south of 43.9°N. Curiously, at approximately 44.4°N, the high-frequency wind solution has near-zero K_1 amplitude (Fig. 2h), while both the HF radar (Fig. 2b) and the daily averaged wind solution (Fig. 2e) have local maxima in K_1 amplitudes. It is possible that surface flow generated by diurnal wind variability near 44.4°N opposes tidal currents in that area. Perlin et al. (2004) showed that in a number of atmospheric models, the accuracy of wind variability in the diurnal band may be limited. Despite the inconsistency between observed and modeled K_1 estimates from HF radar at the WIN location, we may conclude that the surface current response to the diurnal wind variability may explain observed variability in some parts of the coastal ocean off Oregon.

The high-frequency wind solution was also analyzed at the O_1 frequency and results (not shown) were similar to the O_1 analysis of the daily averaged wind solution.

HF radar data and model results were similarly analyzed for the P_1 and Q_1 frequencies. Amplitudes were less than 0.02 m s^{-1} and greatest over the Heceta Bank area and the tip of Cape Blanco.

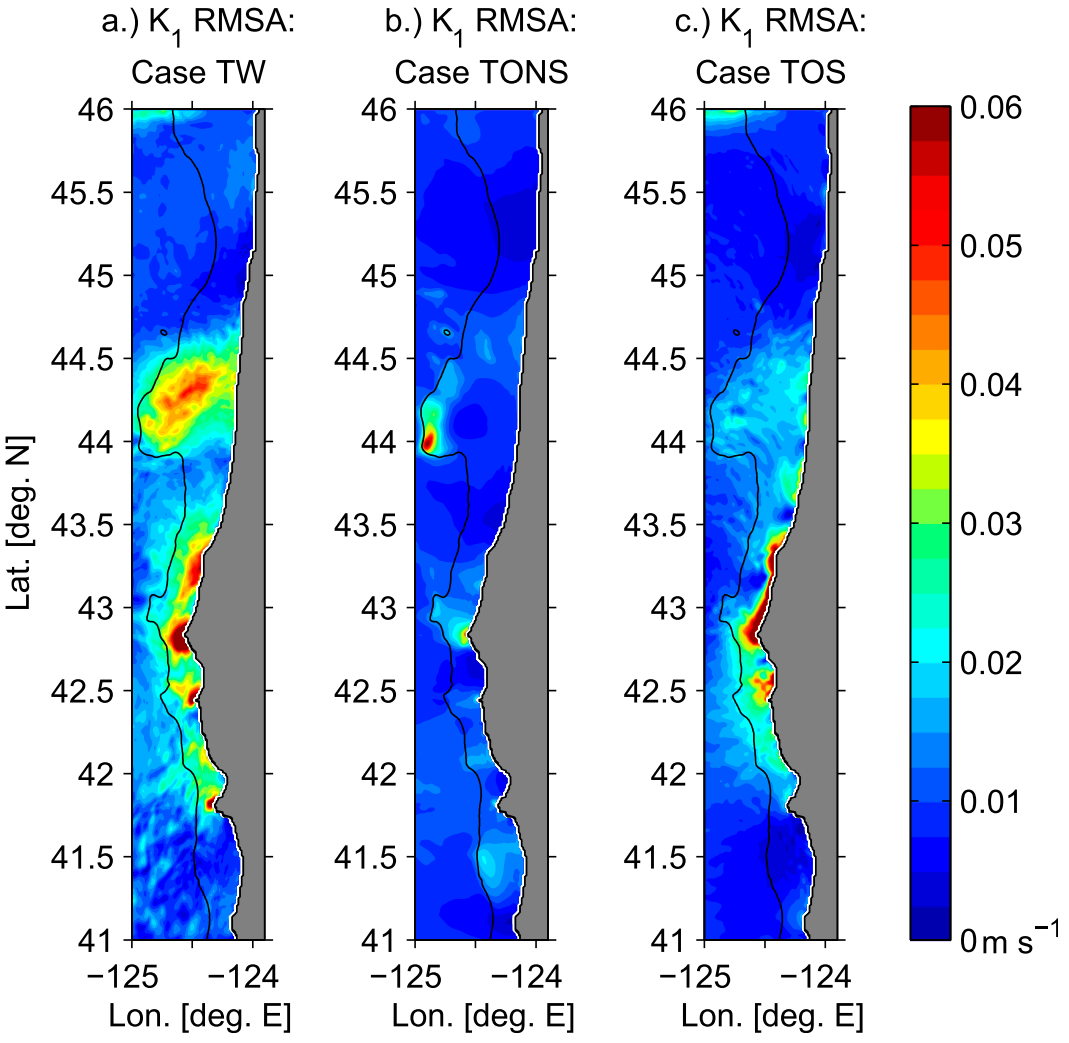

FIG. 5. K_1 RMSA in case (a) TW, (b) TONS, and (c) TOS. The black line marks the 200-m isobath.

4. Sensitivity of the model diurnal tide estimates to ocean background conditions

To gain additional perspective on diurnal tides over the entire Oregon shelf, the root-mean-square K_1 tidal current amplitudes RMSA $= \sqrt{(|\tilde{u}|^2 + |\tilde{v}|^2)/2}$ are computed over the shelf area between 41.5° and 45°N; here $\tilde{u}$ and $\tilde{v}$ are harmonic constants of high-pass-filtered modeled surface currents computed using time series for June and July 2002 (Fig. 5). Diurnal velocity RMSA is found to be very sensitive to details of the background ocean state.

In case TW (forced by atmospheric fields and tides in combination; Fig. 5a), elevated RMSA is found over the long portion of the Oregon shelf (41.7°–44.7°N). Areas of particularly intense RMSA are qualitatively consistent with the results of the HF radar current analysis, described above. The RMSA is largest in the close vicinity of Cape Blanco, reaching 0.18 m s^{-1}.

To test sensitivity of the K_1 tidal velocity to the background ocean conditions, we run case TONS for 20 days and obtain the surface velocity harmonic constants by harmonically analyzing (with T_TIDE) the last 16 days. The RMSA plot corresponding to this case (Fig. 5b) reveals strikingly lower amplitudes than case TW over the entire shelf (including areas north and south of Cape Blanco and the Heceta Bank complex). The only significant area of intensification is at the shelf break between 44° and 44.5°N (the west edge of Heceta Bank). Case TOS is run and processed identically to case TONS. It reveals larger amplitudes than case TONS, but not as large as case TW (Fig. 5c). An exception is the area near and north of Cape Blanco, where additional analysis (not shown) reveals the presence of a tidal-mixed front along the inner shelf. The associated alongshore geostrophic current is advected by the cross-shore tidal currents, which contribute to larger RMSA in the harmonically

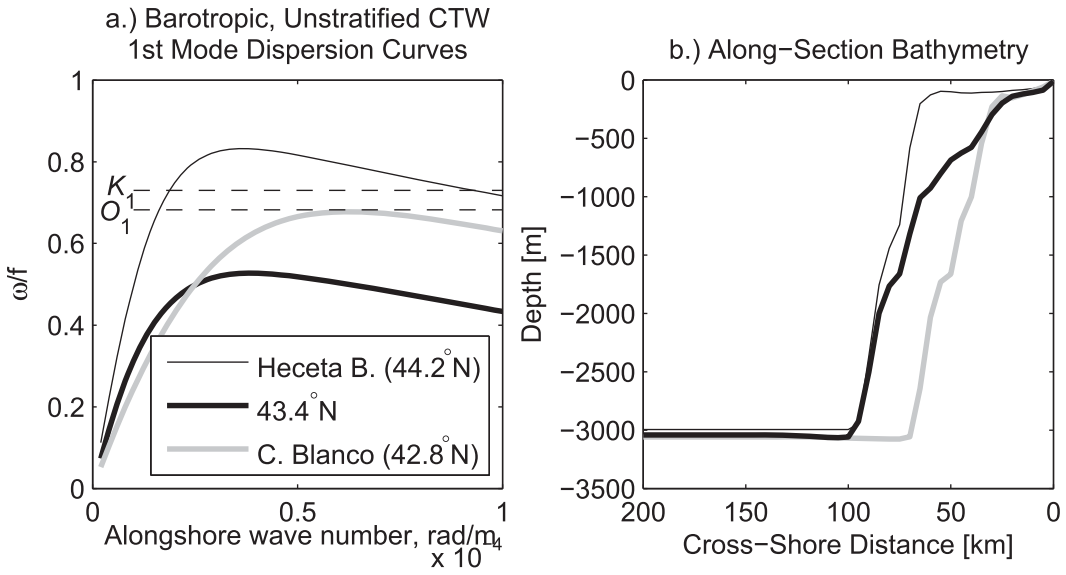

FIG. 6. (a) Dispersion curves for the first-mode coastal-trapped waves at Heceta Bank (44.2°N; thin black line), 43.4°N (thick black line), and Cape Blanco (42.8°N; thick gray line). Dashed black lines indicate the Coriolis-normalized K_1 and O_1 tidal frequencies. (b) Bathymetry along those sections. Note that for eigenvalue analysis, bathymetry has been artificially flattened in the abyssal plane.

analyzed velocity time series. Such a front is not normally formed under time-varying background conditions responding to upwelling- and downwelling-favorable winds and is thus absent from case TW.

Erofeeva et al. (2003) associated intensified tidal velocity amplitudes at the edge of the Heceta Bank with coastal-trapped waves at diurnal frequencies based on the numerical eigenvalue analysis of the shallow-water equations over the alongshore uniform bathymetry (using a bathymetric profile from Heceta Bank). Here, we provide a similar analysis using the bathymetric profiles at 42.8°N (Cape Blanco) and 44.2°N (Heceta Bank) in the regions of larger RMSA. Additionally, we analyzed the section at 43.4°N between Cape Blanco and Heceta Bank. In these computations, a rigid-lid shallow-water model (Brink 1982; Chapman 1983) is utilized. The model variables are assumed to vary proportionally with $\exp[i(\omega t - ly)]$, where l is the alongshore wavenumber component. Dispersion curves for each profile's first wave mode, showing angular frequencies ω/f (normalized by the Coriolis frequency f) as functions of l, are presented in Fig. 6a (and corresponding bathymetric profiles in Fig. 6b). The dispersion curve for Heceta Bank (44.2°N; Fig. 6a, thin black line) crosses the horizontal dashed lines corresponding to the K_1 and O_1 frequencies, indicating that coastal-trapped waves in an unstratified ocean can exist at this location at the diurnal tide frequencies. The dispersion curve for the Cape Blanco profile (42.8°N; Fig. 6a, thick gray line) nearly reaches the O_1 frequency, but does not reach the K_1 frequency. Dispersion curves computed for the gentler slopes south (not shown) and north (Fig. 6a, thick black line) of Cape Blanco show maximums at frequencies much less than diurnal. These are consistent with the generally low K_1 RMSA south of Heceta Bank in case TONS.

The effect of stratification on the dispersion properties of coastal-trapped waves was discussed by Chapman (1983), who showed that with increasing stratification the ascending branch of the dispersion curve (at low wavenumbers) is moved toward higher frequencies (i.e., closer to the diurnal frequencies). Although we do not repeat this analysis here, it is likely that the dispersion curve for 42.8°N that reached the O_1 frequency would rise, reaching the K_1 frequency in case TOS, permitting coastal-trapped waves that would contribute to differences in RMSA between cases TOS and TONS.

To verify basic properties of the diurnal tide as a coastally trapped wave, barotropic (depth averaged) K_1 model tidal currents (case TW) are decomposed into counterclockwise (CCW) and clockwise (CW) rotary components $(\tilde{u} \pm i\tilde{v})/2$ (Pugh 1987). Their amplitude and phase are shown in Fig. 7. The coastal-trapped wave on the Oregon shelf is characterized by CW velocity rotation and south-to-north phase propagation. In Fig. 7, CW amplitudes are generally large where RMSA is large and CCW amplitudes are small everywhere, except around several large capes. Within a few kilometers of Cape Blanco, horizontal barotropic current ellipses are linearly polarized, with the direction of the velocity

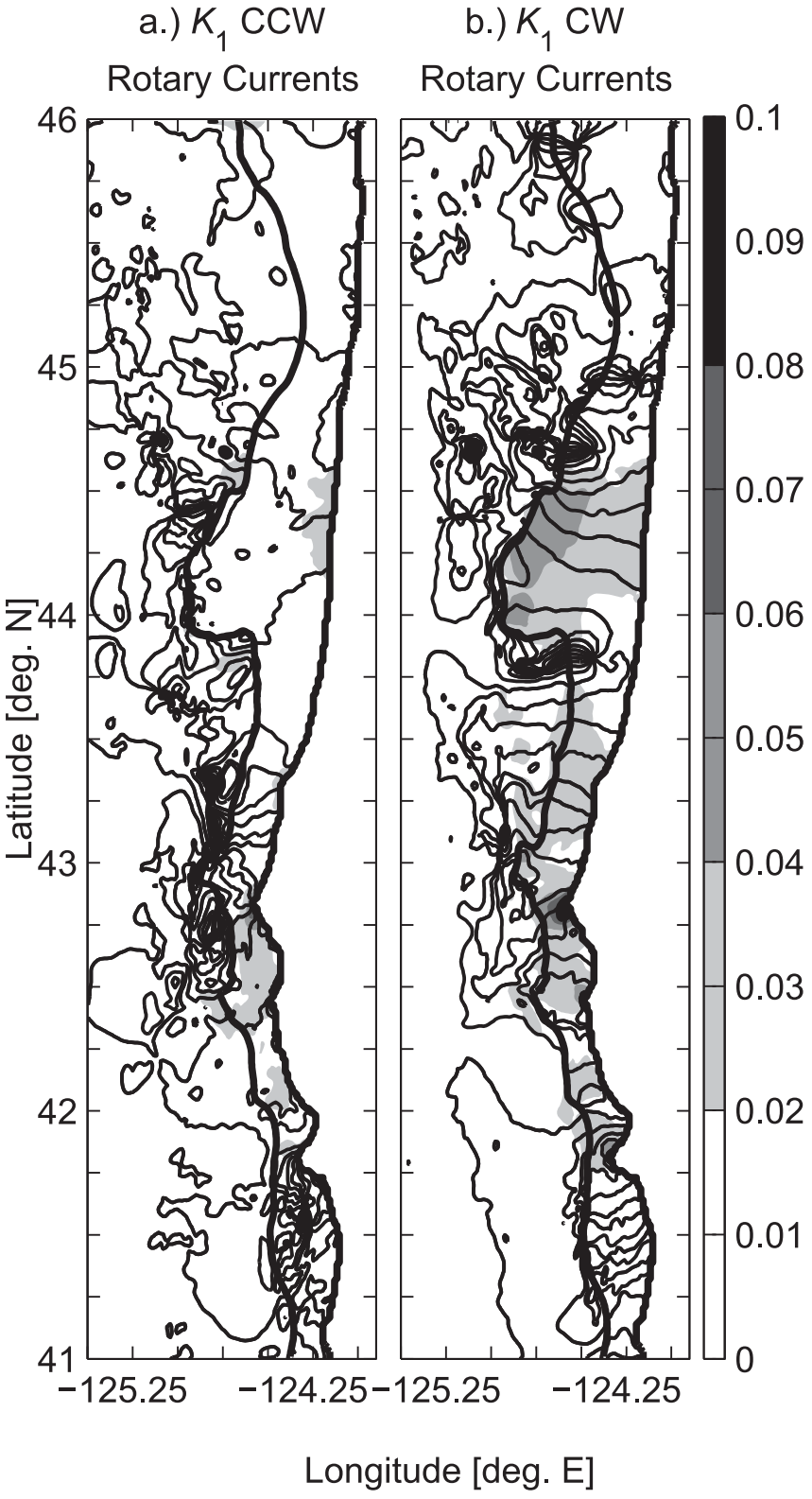

FIG. 7. (a) CCW depth-averaged K_1 rotary currents from case TW. (b) CW depth-averaged K_1 rotary currents from case TW. The thick black lines mark the 200-m isobath and the coast, while the thin black lines mark the rotary current phase (every 30°), and the shading marks rotary current amplitude.

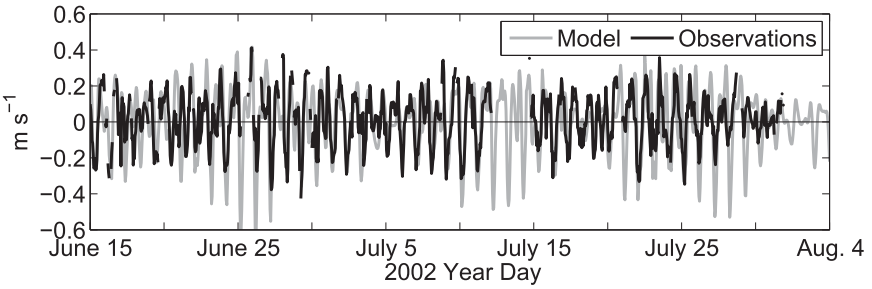

FIG. 8. Time series of HFR-observed (black) and modeled (gray) radial velocity components near Cape Blanco (location marked in Fig. 8).

vector rotation poorly defined. There, maximum CCW and CW amplitudes are approximately equal, close to 0.10 m s^{-1}.

The CW rotary current phase shows northward wave propagation over the shelf in large regions between 42.5° and 43.75°N and 44° and 44.75°N. Between 42.5° and 43.75°N, the K_1 wavelength is about 165 km. Between 44° and 44.75°N (Heceta Bank), the K_1 wavelength is about 250 km.

For the O_1 constituent (not shown), the CW rotary current shows patterns of coastal-trapped waves similar to K_1. The O_1 CW rotary current amplitudes at Heceta Bank and Cape Blanco are up to 0.04 and 0.08 m s^{-1}, respectively.

5. Intensified diurnal tides near Cape Blanco

Data from the HF radar located at the tip of Cape Blanco confirm extreme velocities at diurnal frequency very close to the cape. Figure 8 shows a 50-day time series during June–August 2002 of high-pass-filtered HF radial component velocity (generally in the north–south direction), both observed (black) and modeled (gray), at a point off Cape Blanco (marked in Fig. 9). The chosen location is at the closest radial distance sampled by the

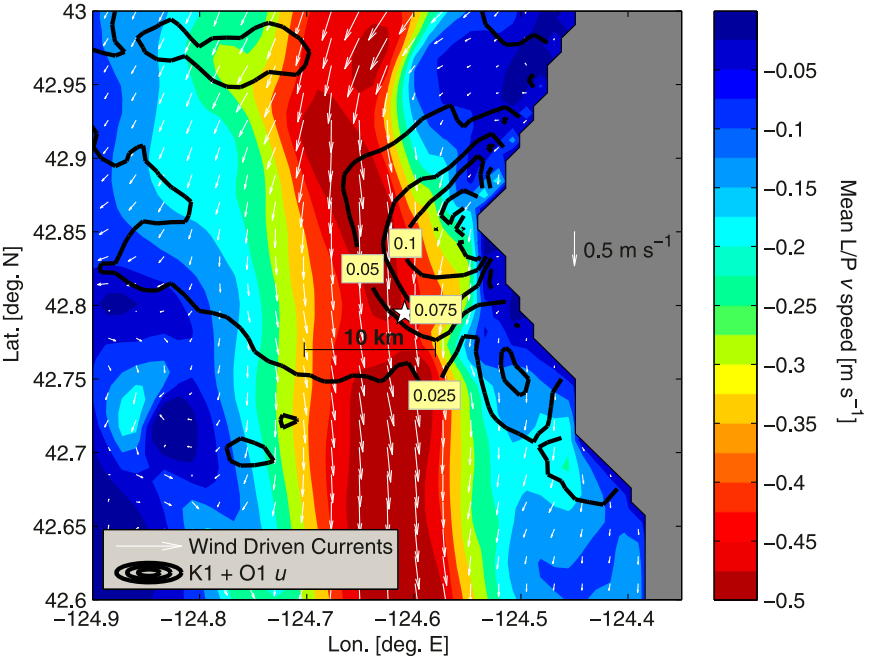

FIG. 9. Color field signifies 40-h low-pass-filtered v from 2300 UTC 25 Jun. Black contours signify $K_1 + O_1$ u (which are in phase during 25–27 Jun) at 0.025, 0.05, 0.075, and 0.1 cm s^{-1}, as computed from high-pass-filtered, harmonically analyzed currents for April–August 2002. The star marks the location of the HFR time series in Fig. 7.

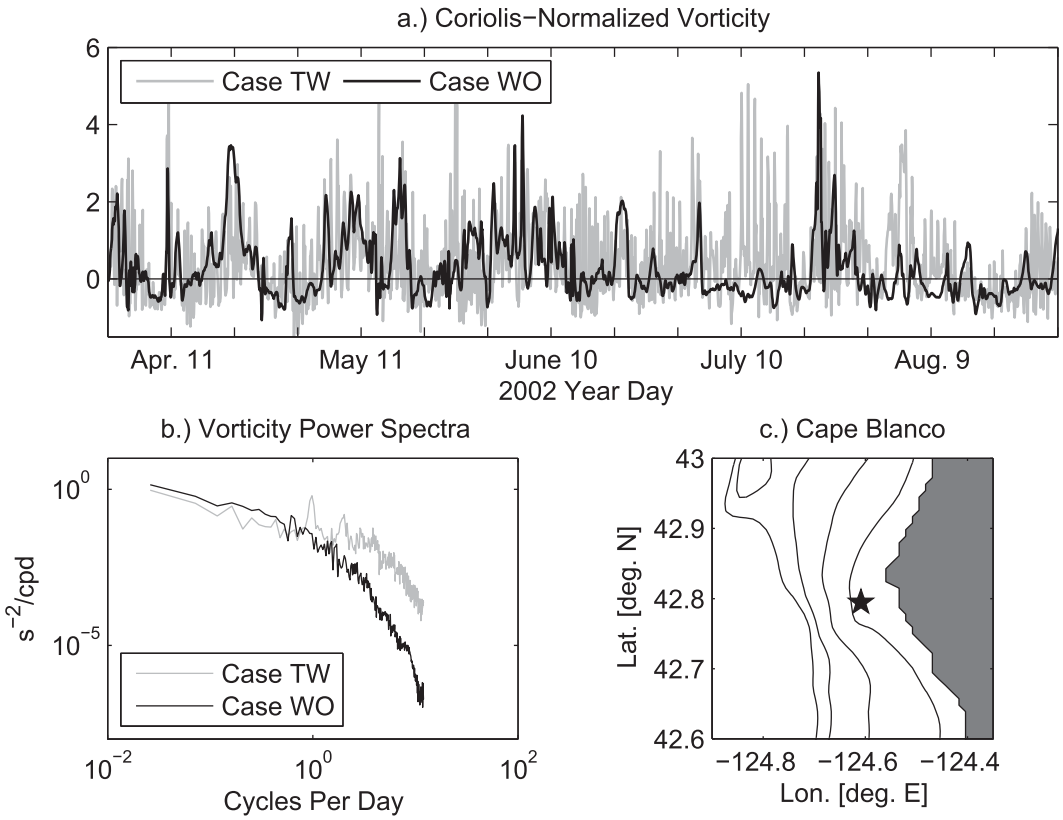

FIG. 10. (a) Time series of Coriolis-normalized relative vorticity (vertical component) from case TW (gray) and WO (black) at the point marked with the star in (c). (b) Spectra of vorticity time series from case TW (gray) and case WO (black), as computed from the entire model run. (c) Close up of Cape Blanco region. Star marks the location of the time series in Fig. 7 and this figure. Black lines mark the 50-, 100-, 150-, and 200-m isobaths.

instrument. Here observed radial speeds may exceed $0.3\,\mathrm{m\,s^{-1}}$. Modeled currents are somewhat larger; the RMS amplitudes of the model and HFR time series are 0.17 and $0.15\,\mathrm{m\,s^{-1}}$, respectively.

The model K_1 amplitudes increase toward the tip of the cape, so it is possible that diurnal tidal currents might exceed $0.3\,\mathrm{m\,s^{-1}}$ closer to the cape. The model predicts the phase of diurnal oscillations remarkably well and also predicts variability in diurnal current amplitudes. These are generally largest when K_1 and O_1 are in phase, during episodes of diurnal spring tides. The period of the diurnal spring–neap cycle is 13.58 days, about 1 day less than the 14.88-day period of the M_2–S_2 spring–neap cycle.

Events of intensified M_2 tide may also be identified in this area. These are intermittent, associated with internal tide motions, and less predictable than diurnal tides. An area of strong barotropic-to-baroclinic M_2 tide conversion on the continental slope, 60 km to the southwest of the cape (see Osborne et al. 2011), may be influencing circulation here. Still, oscillations evident in Fig. 8 are predominantly diurnal.

The presence of a narrow, alongshore coastal jet in the vicinity of this point potentially affects tidal speeds due to the advection of the jet by the cross-shore tidal component. To provide a crude estimate of the significance of this effect, let (u, v) be the orthogonal (cross shore and alongshore) surface tidal velocity components. Let us assume that these evolve in the presence of the steady alongshore background jet $V(x)$. Then the linearized momentum equation would include the u–V advection term: $v_t = -uV_x + \cdots$, where subscripts denote partial derivatives with respect to time t and the cross-shore coordinate x. The magnitude of this term is estimated using model outputs on 2300 UTC 25 June, when both the model and the HF radar show intensified diurnal currents near Cape Blanco (see Fig. 8). During this time, the K_1 and O_1 tides are in phase. In Fig. 9, we show the modeled, instantaneous (subtidal), alongshore surface current (vectors), the magnitude of the instantaneous meridional component V (color), and the amplitude of the average u (zonal) component of surface diurnal tide currents (the K_1 and O_1 constituents combined; black contours). The tidal amplitude estimates have been obtained by harmonic

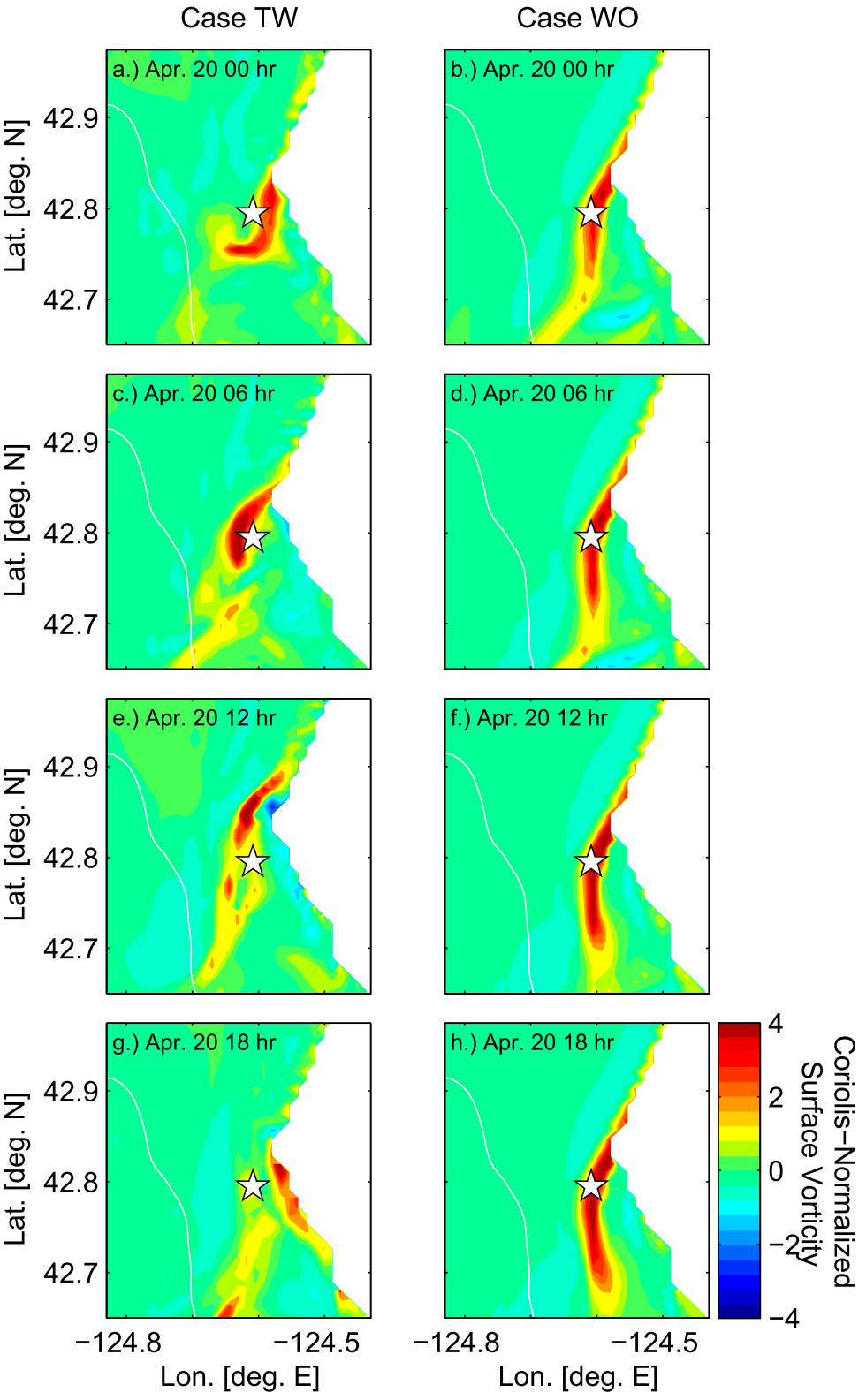

FIG. 11. Instantaneous modeled Coriolis-normalized surface relative vorticity during 20 Apr 2002 for case (left) TW and (right) WO. Horizontal image pairs [i.e., (a) and (b), (c) and (d), (e) and (f), and (g) and (h)] are at the same time for the two cases. Image pairs are separated by 6 h [i.e., (c) and (d) are 2 h after (a) and (b)].

analysis of the 5-month model time series (April–August). The location where velocities (shown in Fig. 8) are sampled is marked by the star. The alongshore velocity in the jet changes between 0.25 and 0.5 m s^{-1} over a distance of 5 km; the corresponding shear is $V_x = 5 \times 10^{-5}$ s^{-1}. The cross-shore advection by the diurnal tidal current with an amplitude of $u = 0.07$ m s^{-1} will provide a contribution to the tidal v amplitude of $uV_x/\omega = 0.05$ m s^{-1}. So, near the cape, this mechanism may contribute 20%–30% of the observed intensified diurnal signal. The rest may be attributed to the coastal-trapped waves and topographic effects.

The same scaling estimates may be applied to other areas of the shelf, in particular, the wide Heceta Bank shelf area. Here, case TOS yields K_1 amplitudes near 0.02 m s^{-1} and case TW near 0.05 m s^{-1}. The 0.03 m s^{-1} increase in the amplitude may be explained easily as the effect of the advection of the upwelling jet by the diurnal tidal current. The HF radar (see Figs. 2 and 3) senses the diurnal tide influenced by this advection.

In addition to being a site with strong tides, Cape Blanco is a separation point for the equatorward coastal jet (Barth et al. 2000; Koch et al. 2010; Kurapov et al. 2011). Energetic tides here may contribute to eddy dynamics and modify cross-shelf transport. Figure 10a shows the time series of the model-derived relative vorticity (vertical component) normalized by the Coriolis parameter, $f^{-1}(\partial v/\partial x - \partial u/\partial y)$ (where u and v are full surface currents), in cases TW (gray) and WO (winds only; black), sampled at the same point as above (see also map in Fig. 10c) and plotted for the entire model run. Case TW shows periodic high-frequency variability in normalized vorticity with peak values exceeding 2, suggesting strongly nonlinear flows. Vorticity spectra (Fig. 10b) confirm that case TW (gray) has more power at higher frequencies than case WO (black), with peaks appearing at 1 and 2 cpd, corresponding to diurnal and semidiurnal tides. Also, the Coriolis-normalized vorticity in case TW shows spatiotemporal variability not seen in case WO. As an example, we show instantaneous maps of vorticity every 6 h on 20 April 2002 (Fig. 11). On this date, the location of frontal structures in cases TW and WO are still similar (after a 20-day spinup from the same initial conditions). Both cases show large vorticity near Cape Blanco, but the tide acts to fundamentally change the model kinematics. In the vicinity of Cape Blanco, the diurnal tide may displace the jet (identified by the patch of large positive vorticity) by as much as 10 km over one tidal cycle (see Fig. 11, left). In comparison, the vorticity field in case WO is relatively steady during this time period (Fig. 11, right). Additional studies will be needed to describe this tidal modulation in more detail and understand mechanisms that may influence jet separation at Cape Blanco and other large capes along the U.S. West Coast (Strub et al. 1991).

6. Summary

Analyses of HF radar surface current data confirm areas of intensified diurnal tidal currents along the Oregon coast. In the vicinity of Cape Blanco, where observed diurnal currents exceed 0.3 m s^{-1}, the currents may be a combination of coastal-trapped waves and advection of the subtidal, wind-driven coastal jet by the tidal currents. The latter mechanism may contribute more than 50% to the diurnal tide current amplitudes over the wider part of the Oregon shelf (Heceta Bank complex).

Our study reveals the effect of the linearized advection on diurnal current amplitudes at the surface on average over the summer season. In future studies, it would be interesting to learn how this effect extends through the water column and whether changes in the strength of the subtidal current influence diurnal current amplitudes on temporal scales from days to seasonal.

Diurnal wind variability also contributes to elevated diurnal surface current amplitudes, in particular, in areas where the strong upwelling jet is found. It is possible that atmospherically driven diurnal ocean variability in the area of the jet is also in part determined by the advection of the alongshore coastal jet by wind-driven diurnal motions.

The 1-km resolution model describes diurnal tide variability in the vicinity of Cape Blanco qualitatively correctly and accurately predicts the timing of intensified diurnal tide events. These come during periods of the diurnal spring tide, when the K_1 and O_1 tides are in phase. Variability in the ocean response from one spring tide period to another may be affected by intermittent semidiurnal internal tides and the intensity of the coastal jet. The ocean model also identifies areas of locally intensified diurnal tidal currents in the vicinity of a number of smaller capes. Additional studies will be needed to understand details of three-dimensional tidally driven circulation around Cape Blanco, as influenced by headland topography (e.g., Signell and Geyer 1991; Geyer 1993; McCabe et al. 2006).

Strong tidal modulation of surface currents in the vicinity of the capes may affect material transports, in particular larvae dispersion. Areas of high larvae retention rates have been proposed as marine protected areas. Numerical simulations of larvae dispersion (e.g., Kim and Barth 2011) should account for tidal variability to more accurately predict particle movement and retention in shallow coastal environments.

Acknowledgments. This research was supported by the National Science Foundation (Grants OCE-0000734,

OCE-0648314, and OCE-1030922), the Office of Naval Research Physical Oceanography Program (Grants N000140810942 and N000141010745), National Oceanic and Atmospheric Administration (NOAA) Grant NA11NOS0120036, NOAA–CIOSS, and NOAA–IOOS (NANOOS). The authors thank J. A. Barth, M. S. Hoecker-Martinez, R. M. Samelson, and S. H. Suanda for their helpful discussions.

REFERENCES

Barth, J. A., S. D. Pierce, and R. L. Smith, 2000: A separating coastal upwelling jet at Cape Blanco, Oregon and its connection to the California Current System. *Deep-Sea Res. II,* **47,** 783–810, doi:10.1016/S0967-0645(99)00127-7.

Brink, K. H., 1982: A comparison of long coastal trapped wave theory with observations off Peru. *J. Phys. Oceanogr.,* **12,** 897–913, doi:10.1175/1520-0485(1982)012<0897:ACOLCT>2.0.CO;2.

Cartwright, D. E., 1969: Extraordinary tidal currents near St. Kilda. *Nature,* **223,** 928–932, doi:10.1038/223928a0.

Chapman, D. C., 1983: On the influence of stratification and continental shelf and slope topography on the dispersion of subinertial coastally trapped waves. *J. Phys. Oceanogr.,* **13,** 1641–1652, doi:10.1175/1520-0485(1983)013<1641:OTIOSA>2.0.CO;2.

Crawford, W. R., and R. E. Thomson, 1982: Continental shelf waves of diurnal period along Vancouver Island. *J. Geophys. Res.,* **87,** 9516–9527, doi:10.1029/JC087iC12p09516.

——, and ——, 1984: Diurnal-period continental shelf waves along Vancouver Island: A comparison of observation with theoretical models. *J. Phys. Oceanogr.,* **14,** 1629–1646, doi:10.1175/1520-0485(1984)014<1629:DPCSWA>2.0.CO;2.

Cummins, P. F., D. Masson, and M. G. G. Foreman, 2000: Stratification and mean flow effects on diurnal tidal currents off Vancouver Island. *J. Phys. Oceanogr.,* **30,** 15–30, doi:10.1175/1520-0485(2000)030<0015:SAMFEO>2.0.CO;2.

Egbert, G. D., and S. Y. Erofeeva, 2002: Efficient inverse modeling of barotropic ocean tides. *J. Atmos. Oceanic Technol.,* **19,** 183–204, doi:10.1175/1520-0426(2002)019<0183:EIMOBO>2.0.CO;2.

Erofeeva, S. Y., G. D. Egbert, and P. M. Kosro, 2003: Tidal currents on the central Oregon shelf: Models, data, and assimilation. *J. Geophys. Res.,* **108,** 3148, doi:10.1029/2002JC001615.

Geyer, W. R., 1993: Three-dimensional tidal flow around headlands. *J. Geophys. Res.,* **98,** 955–966, doi:10.1029/92JC02270.

Hayes, S. P., and D. Halpern, 1976: Observations of internal waves and coastal upwelling on the Oregon coast. *J. Mar. Res.,* **34,** 247–267.

Hodur, R. M., 1997: The Naval Research Laboratory's Coupled Ocean/Atmosphere Mesoscale Prediction System (COAMPS). *Mon. Wea. Rev.,* **125,** 1414–1430, doi:10.1175/1520-0493(1997)125<1414:TNRLSC>2.0.CO;2.

Kalnay, E., and Coauthors, 1996: The NCEP/NCAR 40-Year Reanalysis Project. *Bull. Amer. Meteor. Soc.,* **77,** 437–471, doi:10.1175/1520-0477(1996)077<0437:TNYRP>2.0.CO;2.

Kim, S., and J. A. Barth, 2011: Connectivity and larval dispersal along the Oregon coast estimated by numerical simulations. *J. Geophys. Res.,* **116,** L06002, doi:10.1029/2010JC006741.

Koch, A. O., A. L. Kurapov, and J. S. Allen, 2010: Near-surface dynamics of a separated jet in the coastal transition zone off Oregon. *J. Geophys. Res.,* **115,** C08020, doi:10.1029/2009JC005704.

Kosro, P. M., 2005: On the spatial structure of coastal circulation off Newport, Oregon, during spring and summer 2001 in a region of varying shelf width. *J. Geophys. Res.,* **110,** C10S06, doi:10.1029/2004JC002769.

——, W. T. Peterson, B. M. Hickey, R. K. Shearman, and S. D. Pierce, 2006: Physical versus the biological spring transition: 2005. *Geophys. Res. Lett.,* **33,** L22S03, doi:10.1029/2006GL027072.

Kovalev, P. D., and A. B. Rabinovich, 1980: Bottom measurements of tidal currents in the southern part of the Kuril-Kamchatka Trench. *Oceanology,* **20,** 294–299.

Kurapov, A. L., G. D. Egbert, J. S. Allen, R. N. Miller, S. Y. Erofeeva, and P. M. Kosro, 2003: The M_2 internal tide off Oregon: Inferences from data assimilation. *J. Phys. Oceanogr.,* **33,** 1733–1757, doi:10.1175/2397.1.

——, D. Foley, P. T. Strub, G. D. Egbert, and J. S. Allen, 2011: Variational assimilation of satellite observations in a coastal ocean model off Oregon. *J. Geophys. Res.,* **116,** C05006, doi:10.1029/2010JC006909.

Liu, W. T., 2002: Progress in scatterometer application. *J. Oceanogr.,* **58,** 121–136, doi:10.1023/A:1015832919110.

——, and X. Xie, 2001: Improvement in spacebased scatterometers and increased scientific impact in the past decade. *Proc. Oceans 2001,* Vol. 1, Honolulu, HI, Marine Technology Society, 626–630.

Maturi, E., A. Harris, C. Merchant, J. Mittaz, B. Potash, W. Meng, and J. Sapper, 2008: NOAA's sea surface temperature products from operational geostationary satellites. *Bull. Amer. Meteor. Soc.,* **89,** 1877–1888, doi:10.1175/2008BAMS2528.1.

McCabe, R. M., P. MacCready, and G. Pawlak, 2006: Form drag due to flow separation at a headland. *J. Phys. Oceanogr.,* **36,** 2136–2152, doi:10.1175/JPO2966.1.

Odamaki, M., 1994: Tides and tidal currents along the Okhotsk coast of Hokkaido. *J. Oceanogr.,* **50,** 265–279, doi:10.1007/BF02239517.

Oliger, J., and A. Sundström, 1978: Theoretical and practical aspects of some initial boundary value problems in fluid dynamics. *SIAM J. Appl. Math.,* **35,** 419–446, doi:10.1137/0135035.

Osborne, J. J., A. L. Kurapov, G. D. Egbert, and P. M. Kosro, 2011: Spatial and temporal variability of the M_2 internal tide generation and propagation on the Oregon shelf. *J. Phys. Oceanogr.,* **41,** 2037–2062, doi:10.1175/JPO-D-11-02.1.

Pawlowicz, R., B. Beardsley, and S. Lentz, 2002: Classical tidal harmonic analysis including error estimates in MATLAB using T_TIDE. *Comput. Geosci.,* **28,** 929–937, doi:10.1016/S0098-3004(02)00013-4.

Perlin, N., R. M. Samelson, and D. B. Chelton, 2004: Scatterometer and model wind and wind stress in the northern California coastal zone. *Mon. Wea. Rev.,* **132,** 2110–2129, doi:10.1175/1520-0493(2004)132<2110:SAMWAW>2.0.CO;2.

Pugh, D. T., 1987: *Tides, Surges, and Mean Sea-Level*. John Wiley and Sons, 472 pp.

Rabinovich, A. B., and A. E. Zhukov, 1984: Tidal oscillations on the shelf of Sakhalin Island. *Oceanology,* **24,** 184–189.

——, and R. E. Thomson, 2001: Evidence of diurnal shelf waves in satellite-tracked drifter trajectories off the Kuril Islands. *J. Phys. Oceanogr.,* **31,** 2650–2668, doi:10.1175/1520-0485(2001)031<2650:EODSWI>2.0.CO;2.

Saraceno, M., P. T. Strub, and P. M. Kosro, 2008: Estimates of sea surface height and near-surface alongshore coastal currents from combinations of altimeters and tide gauges. *J. Geophys. Res.,* **113,** C11013, doi:10.1029/2008JC004756.

Shchepetkin, A. F., and J. C. McWilliams, 2005: The Regional Oceanic Modeling Systems (ROMS): A split-explicit, free-surface, topography-following-coordinate oceanic model. *Ocean Modell.,* **9,** 347–404, doi:10.1016/j.ocemod.2004.08.002.

Signell, R. P., and W. R. Geyer, 1991: Transient eddy formation around headlands. *J. Geophys. Res.,* **96,** 2561–2575, doi:10.1029/90JC02029.

Smith, R. L., A. Huyer, and J. Fleischbein, 2001: The coastal ocean off Oregon from 1961 to 2000: Is there evidence of climate change or only of Los Niños? *Prog. Oceanogr.,* **49,** 63–93, doi:10.1016/S0079-6611(01)00016-7.

Strub, P. T., P. M. Kosro, A. Huyer, and C. Collaborators, 1991: The nature of the cold filaments in the California Current System. *J. Geophys. Res.,* **96,** 14 743–14 768, doi:10.1029/91JC01024.

Torgrimson, G. M., and B. M. Hickey, 1979: Barotropic and baroclinic tides over the continental slope and shelf off Oregon. *J. Phys. Oceanogr.,* **9,** 945–961, doi:10.1175/1520-0485(1979)009<0945:BABTOT>2.0.CO;2.

Yefimov, V. V., and A. B. Rabinovich, 1980: Resonant tidal currents and their relation to continental shelf waves of the northwestern Pacific Ocean. *Izv. Atmos. Ocean. Phys.,* **16,** 805–812.